Chalcogenide Letters

Tech Science Press

http://doi.org/10.32604/cl.2026.087654

REVIEW

Emerging MoS_2-Based Composite Approaches for the Detection of SF_6 Decomposition Gases: A Review

Huo Ye[1], Jiantong Li[2] and Lingna Xu[3,*]

[1]School of Materials and Energy, Southwest University, Chongqing, China
[2]School of Traditional Chinese Medicine, Chongqing University of Chinese Medicine, Chongqing, China
[3]College of Engineering and Technology, Southwest University, Chongqing, China
*Corresponding Author: Lingna Xu. Email: lingnaxu@swu.edu.cn

Received: 20 June 2026; Accepted: 19 August 2026; Published: 18 September 2026

ABSTRACT: SF_6 is the primary insulating and arc extinction medium in gas-insulated switchgear (GIS). Sulfur hexafluoride (SF_6) decomposes to create diagnostic markers, such as sulfur dioxide (SO_2), thionyl fluoride (SOF_2), and hydrogen sulfide (H_2S) when electrical problems occur, such as partial discharge and local overheating. Accurate quantification of these fault-marker gases is important for the early identification of insulation defects and the condition assessment of SF_6-insulated equipment. Molybdenum disulfide (MoS_2) is a well-known and atomically thin van der Waals semiconductor that has attracted considerable attention as a platform for gas-sensing applications. This is due to its large accessible surface area, ability to tune its bandgap using a gate, and its good charge transfer properties. Gas adsorption induces charge transfer and redistributes charge carriers in MoS_2, thereby reorganizing surface energy levels and changing its electrical properties. This review summarizes recent advances in MoS_2-based sensing materials for the detection of SF_6 decomposition gases. This review examined three key ways to improve performance: modifying the atomic lattice, surface modification, and constructing heterojunction composites. Each of these strategies contributes to improving detection capabilities in a different way. Beyond decomposition-gas detection, ppm-scale moisture sensing and SF_6 leakage monitoring are also briefly compared as complementary functions required for automated GIS condition monitoring. The review evaluates the effectiveness of these sensing materials for detecting SO_2 and thionyl fluoride SOF_2 and outlines future research directions.

KEYWORDS: MoS_2; SF_6 decomposition gases; gas sensor; DFT

1 Introduction

GIS has become an integral part of modern high-voltage power transmission and distribution infrastructure, thanks to its compact size, reliable operation, and excellent insulation properties. SF_6 is the most commonly used insulating agent and arc-quenching agent in GIS power systems [1]. Its high electronegativity and chemical stability support reliable operation. When SF_6 is subjected to sustained high power stress, partial discharge conditions, and elevated operating temperatures, its breakdown products are unique. The degradation products also reveal how well-protected the device is internally, which is a key indicator of its operational reliability. In the presence of electrical arcs, partial discharges, and thermal stress, SF_6 produces a range of trace gases, including sulfur dioxide, thionyl fluoride, sulfuryl fluoride, and hydrogen sulfide. The composition, concentration, and relative ratios of SF_6 decomposition products vary with the type and severity of insulation faults [2]. Accurate quantification of these products therefore

provides an important basis for early fault identification and condition assessment of GIS equipment [3,4]. However, decomposition-gas analysis alone does not provide a complete assessment of GIS operating conditions. Moisture monitoring evaluates gas quality and condensation-related risks, whereas pressure, density, ambient SF_6 concentration, and infrared measurements are used to detect or localize leakage; together, these complementary measurements support condition-based maintenance and substation automation [5,6]. Common methods for analyzing SF_6 decomposition gases include gas chromatography, infrared absorption spectroscopy, and electrochemical sensing [7,8]. These techniques can provide reliable measurements, but their high capital and operating costs and complex instrumentation can hinder continuous online deployment. In stark contrast, solid-state semiconductor gas sensors have become increasingly popular in recent years, primarily due to their compact size, fast response time, and ease of integration with miniaturized electronics. The main issue with conventional metal oxide semiconductor sensor layers is that they operate at high temperatures, which can result in cross-sensitivity in complex gas mixtures. It has become more difficult to make them widely popular in many applications.

In this context, MoS_2 has emerged as a promising next-generation sensing platform. The sandwich arrangement of atoms creates a very high surface-to-volume ratio, and the bandgap, which varies depending on the number of layers, is roughly 1.2 eV in bulk and 1.8 eV in the monolayer limit. In addition to its inherent properties, MoS_2 is remarkably receptive to post-synthesis modifications, including the introduction of point defects, doping with substitutional atoms, decoration with metal particles, and formation of semiconductor heterojunctions [9–11]. These changes can substantially boost its affinity for specific analytes and improve signal contrast. Previous reviews have mainly addressed SF_6 decomposition mechanisms and diagnostic or detection methods [12], while Qian et al. summarized MoS_2 morphology and selected theoretical and experimental sensing studies available at that time [13]. However, an updated and integrated comparison of lattice substitution, surface functionalization, and heterojunction/composite construction, linking first-principles predictions with experimentally demonstrated devices, remains limited. The present review addresses this more specific gap. These combined properties position MoS_2 as a promising low-power sensing material for miniaturized online GIS monitoring at room temperature. The review first summarizes the composition of SF_6 decomposition gases and their diagnostic importance. It then details the intrinsic sensing mechanism of MoS_2-based materials, before examining three main modification techniques that have been used to overcome the weak intrinsic adsorption of pristine MoS_2. The recent advances in sensing applications targeting the four main fault gases are comprehensively reviewed, covering both experimental and computational perspectives. Finally, this study identifies key challenges and future research directions to guide the design of new sensing materials.

2 SF_6 Decomposition Gases and Their Detection Principles

2.1 Composition of SF_6 Decomposition Gases

SF_6 is the most commonly used dielectric material in GIS installations [14]. During operation, the internal insulation system may develop defects, including contamination by metallic particles, electrode protrusions, and voids, which can trigger partial discharges and decompose SF_6. The reactive sulfur-fluorine intermediates combine readily with trace amounts of moisture and oxygen to produce a variety of chemically stable byproducts. The presence of arcing, even localized heating, can generate H_2S as a further breakdown product. How products are distributed can vary widely depending on the type of fault. H_2S detected only under thermal-fault conditions, making it a strong marker to differentiate between different types of faults [15–18]. Fig. 1 shows the best adsorption geometries of representative decomposition gases on the pristine MoS_2 basal plane.

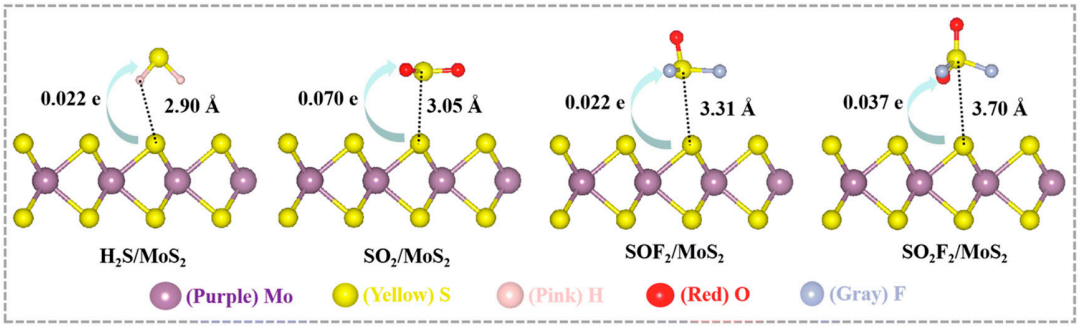

Figure 1: Optimized structures of adsorbed gases on pristine MoS_2. Green directional lines show the number of transferred charges, and dashed lines represent the adsorption distance. Reproduced from Ref. [19].

2.2 Sensing Mechanism of MoS_2-Based Sensors

MoS_2 is a member of the family of two-dimensional transition metal dichalcogenides (tMDs). MoS_2 has a layered S–Mo–S sandwich structure and a large accessible surface area, making it attractive for gas-sensing applications. In a MoS_2-based resistive sensor, the signal is generated by how adsorbates redistribute charge. Molecules landing on the base plane or edge positions exchange electrons with the lattice, which shifts the local Fermi level and causes measurable changes in sheet resistance or contact potential. Previous first-principles density functional theory (DFT) studies have examined these gas–surface interactions at the atomic level. Key descriptors include adsorption energy, which quantifies binding stability, and net Mulliken or Bader charge transfer (ΔQ), which describes the magnitude and direction of electron transfer upon gas adsorption [20]. The MoS_2 structure is appealing, but it only modestly interacts with most of the SF_6 decomposition products. The interactions are all within the van der Waals physisorption regime. So, we can get practical sensor performance through substitutional doping, surface modification, or building composite interfaces [13].

3 Strategies for Enhancing Gas Sensing Performance of MoS_2

3.1 Intrinsic Structure Modification

Surveys of pristine MoS_2 geometry consistently show that the native basal surface has low affinity for SF_6 decomposition products (−0.21 to −0.33 eV). The interaction is too weak to induce substantial charge transfer or a readily detectable resistance change. This limitation motivates lattice-level modification, often by substituting foreign atoms at Mo or S sites. The replacements set up centers that simultaneously change the local electrostatic landscape and forge new paths for orbital hybridization, turning what was once an inert basal plane into an active surface that can engage in directional, covalent-like interactions with target molecules [21,22].

Among non-metallic dopants, the introduction of silicon at sulfur lattice sites has been investigated by Gui et al. [23], who examined the electronic structure, binding energy, charge redistribution, and electron-density difference for the adsorption of hydrogen sulfide and sulfur fluoride (Fig. 2a,b). The calculations reveal that adding silicon significantly increases the surface activity of the MoS_2 plane compared to its undoped state. Phosphorus substitution provides another route to enhance H_2S sensitivity. Szary [24] performed a comparative DFT analysis of P-, Cl-, and Ge-doped MoS_2 and discussed electron-beam irradiation as a possible route for dopant incorporation. It was determined that while the improvements from Ge and Cl substitution were marginal, P doping amplified the charge transfer that happens when H_2S is adsorbed by 354% compared to pristine MoS_2. The use of B substitution has gained interest due to its electron-poor

coordination environment. Tursun et al. [19] found that B@MoS_2 has adsorption energies ranging from −1.67 to −0.39 eV, with adsorbed distances ranging from 1.60 to 3.24 Å, along with measurable charge transfer and amplified sensor signal. Hou et al. [25] investigated the adsorption of three representative SF_6 decomposition products—SO_2, SOF_2, and SO_2F_2—on Ga-doped MoS_2 (Fig. 2(a1–c2)). The calculations indicated that Ga-MoS_2 interacts more strongly with SO_2 and SO_2F_2 than with SOF_2, highlighting the importance of analyte-specific dopant selection. These theoretical descriptors indicate relative adsorption and sensing tendencies but do not establish a quantitative relationship between gas concentration and electrical sensor output. A practical Ga-MoS_2 sensor would therefore require experimental calibration using certified SO_2, SOF_2, and SO_2F_2 mixtures at several known concentrations in an SF_6 matrix, followed by the construction and independent validation of single- and multicomponent response–concentration models that account for the SF_6 background and cross-gas interference. Matrix-specific spectroscopic studies have demonstrated that such quantitative calibration is feasible, but an equivalent calibration has not yet been reported for a Ga-MoS_2 sensing device [26,27].

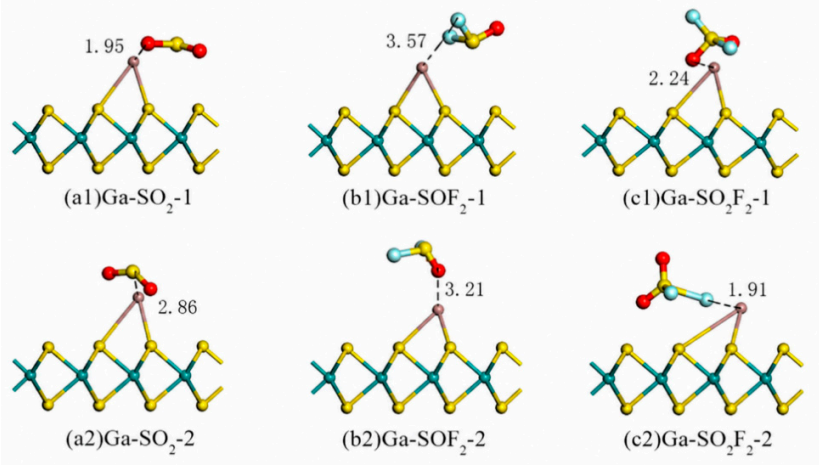

Figure 2: Two optimized adsorption configurations of (**a1**,**a2**) SO_2, (**b1**,**b2**) SOF_2, and (**c1**,**c2**) SO_2F_2 on Ga–MoS_2. Adapted from Ref. [25].

Subsequent studies examined how different concentrations of doping agents impacted MoS_2's sensitivity to decomposition products generated from SF_6. Wei et al. [28] reported that Ni-doped MoS_2 shows promise for the simultaneous detection of H_2S and SO_2. They also discovered that both gases engage in strong, directional surface interactions at the Ni site, with adsorption energies of −1.319 eV and −1.382 eV, respectively. The corresponding TDOS and PDOS results are shown in Fig. 3. In order to bring the model more in line with real-world GIS conditions, Li et al. [29] extended the Pd–MoS_2 monolayer model to include both single- and dual-molecule configurations. They found that each Pd site could only accommodate one gas molecule at a time, and that both SOF_2 and SO_2F_2 chemisorbed at the Pd center, indicating a preference for fluorinated species. Gui et al. [30] explored how Co-substituted MoS_2 can be applied to detect SOF_2 and SO_2F_2. The interaction between the two analytes was positive, resulting in adsorption energies of −1.765 eV and −2.390 eV. The band gap increased upon adsorption, leading to a dramatic drop in conductivity, which reinforced the notion of chemical bonding and a distinct resistance effect. Chen et al. [31] conducted a parallel comparison of platinum-substituted and gold-substituted monolayers of MoS_2 for SO_2, SOF_2, and SO_2F_2. The study revealed that Pt-based systems exhibited strong chemisorption, accompanied by significant charge redistribution for both SO_2 and SOF_2, while Au systems relied on physisorption. Li et al. [32] conducted the hydrothermal step study to incorporate Sc substitution into MoS_2. They built

a four-gas DFT model covering H_2S, SO_2, SOF_2, and SO_2F_2. Binding affinities followed this hierarchy: SO_2F_2 > SOF_2 > SO_2 > H_2S. The relatively weak interaction between H_2S offers a useful benchmark for co-doping strategies that aim to enhance affinity for sulfide species. Collectively, the diverse selectivity profiles observed across different metal substituents highlight a promising approach for targeted analyte discrimination based on deliberate choice of dopants.

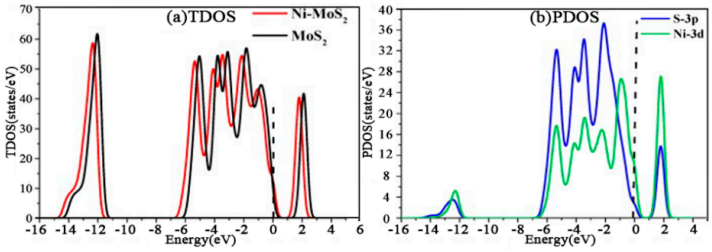

Figure 3: (**a**) The TDOS of Ni-MoS_2; (**b**) the PDOS of Ni-MoS_2, the dashed lines represent the Fermi level. Adapted from Ref. [28].

The focus has shifted from computational prediction to the fabrication of sensing devices in studies on Nickel, Cobalt, and Palladium-substituted systems. For SO_2, Zhang et al. [33] prepared $Mo_{0.9}M_{0.1}S_2$ (where M = Ni, Fe, Co) nanoflowers via a one-step hydrothermal method (Fig. 4a,b) and deposited them onto interdigitated electrodes patterned on flame-retardant-4 (FR-4) epoxy substrates to fabricate thin-film sensors. Across a dynamic range of 0.25 ppm to 4000 ppm at ambient temperature, the Ni-substituted variant provided the most notable figures of merit: a limit of detection of 250 ppb, a response signal of 7.4% at 5 ppm SO_2, response and recovery times of 50 and 56 s, performance stability sustained over 35 days, and markedly improved discrimination against interferents like NO_2, NH_3, CO, CO_2, and H_2. For sulfur sensing, Verma et al. [34] deposited pristine and Pd-doped MoS_2 thin films on SiO_2/Si wafers via atmospheric pressure chemical vapor deposition (APCVD), then transferred the films to platinum interdigitated electrode (IDE) substrates by surface-energy-assisted wet transfer for dynamic-flow sensing characterization at room temperature (Fig. 4c). The MoS_2 sensor with 5 at% Pd doping exhibited an H_2S response 2.88 times that of pristine MoS_2 at an H_2S concentration of 100 ppm. Its response and recovery times were 45 and 65.8 s, respectively. In addition, it showed high selectivity against coexisting gases, with a limit of detection of 0.3 ppb and a limit of quantification of 0.99 ppb. When the Pd loading was increased to 10 at%, the response decreased from 276.5% to 214%, possibly owing to Pd-cluster agglomeration at excessive doping levels.

In short, computational studies of Ni-, Co-, and Pd-substituted systems revealed a shared sensitization mechanism based on d-orbital-driven chemical bonding, and both Ni- and Pd-containing materials moved on to build experimental SO_2 and H_2S sensors, respectively. However, an important gap remains: no experimental device targeting SOF_2 or SO_2F_2 has yet been reported. Bridging the gap between theoretical predictions and functional prototypes is therefore a priority in this research area.

3.2 Surface Functionalization

This substitution doping will permanently anchor foreign atoms within the MoS_2 lattice, profoundly altering the active-site chemistry based on the coordination environment of the replaced lattice position. Instead of putting the function inside the sheet, a better way is to make the surface functional. Species rooted in place by S-coordination or metal-chalcogen bonds are exposed to incoming gas molecules through their frontier d-orbitals and p-orbitals, driving strong orbital overlap without disturbing the lattice. The type, loading, and dispersion of surface modifiers can be controlled through methods such as hydrothermal

reduction and wet impregnation. Because these approaches largely preserve the MoS_2 lattice, interlayer bonding, and mechanical integrity, they are compatible with flexible and ultrathin sensing-film architectures. These benefits collectively demonstrate why surface modification was the first step to create functional prototype sensors in the MoS_2/SF_6 gas detection field, and it remains the most technologically mature way to turn computational predictions into working sensing devices.

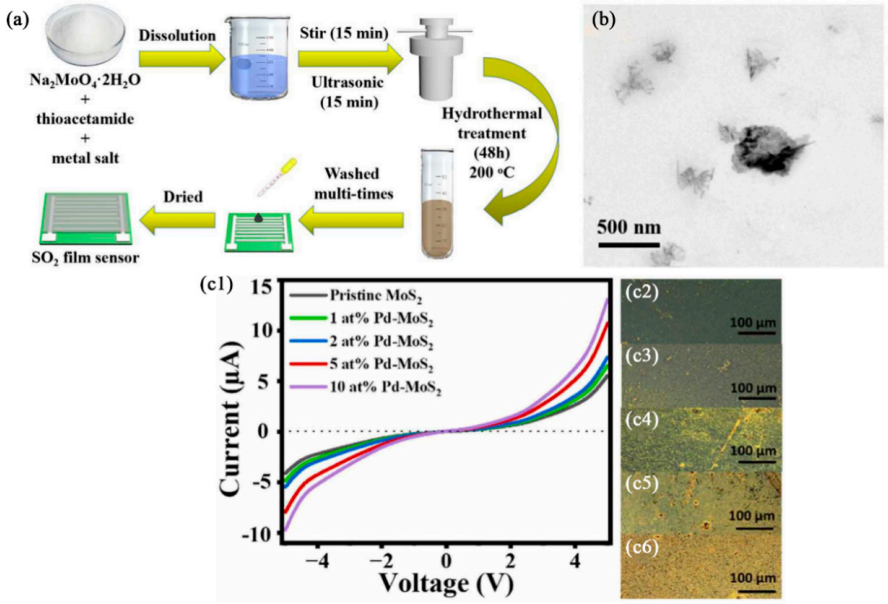

Figure 4: (**a**) Schematic illustration of the hydrothermal synthesis of metal-doped MoS_2 nanoflowers and fabrication of an SO_2 film sensor by drop casting; (**b**) TEM image of the Ni-doped MoS_2 nanoflower sample; (**c1**) current–voltage (I–V) characteristics of pristine MoS_2 and MoS_2 thin films doped with 1, 2, 5, and 10 at% Pd; (**c2**–**c6**) optical micrographs of pristine MoS_2 and MoS_2 thin films doped with 1, 2, 5, and 10 at% Pd, respectively. Panels (**a**,**b**) were adapted from Ref. [33]; panels (**c1**–**c6**) were adapted from Ref. [34].

3.2.1 Noble Metal Nanoparticle Modification

On the theoretical side, Gui et al. [35] extended previous work on SO_2F_2 adsorption on Au-modified MoS_2. Whereas the earlier study considered intact SO_2F_2 configurations and reported physisorption, Gui et al. identified an exothermic dissociative chemisorption configuration in which an S–F bond breaks and an Au–F bond forms. The adsorption energy for one SO_2F_2 molecule was −0.559 eV. The HOMO–LUMO gap increased from 0.290 eV for bare Au–MoS_2 to 0.981 eV after adsorption of one SO_2F_2 molecule. In the two-molecule configuration, only one molecule interacted strongly with the Au site, whereas the second remained weakly adsorbed, and the gap was 0.507 eV. These findings support Au–MoS_2 as a potential adsorbent for SO_2F_2 removal from SF_6-insulated equipment. Gui et al. [36] expanded this line of inquiry to the modification of Pt within the same transition metal dichalcogenide (TMD) family, scaling from single-atom decoration to dual-Pt systems (e.g., Pt_2-MoS_2) to introduce a cooperative multi-site adsorption concept, and comparing single- and dual-Pt exposures of SOF_2 and SO_2F_2. Changes in the HOMO-LUMO gap that occur with adsorption predict measurable changes in conductance for all configurations. The largest variation in the gap is expected to lead to the largest change in conductance.

Qian et al. [37] used first-principles DFT calculations to investigate SOF_2 and SO_2F_2 adsorption and sensing on Pt_3-decorated $MoSe_2$ monolayers. SO_2F_2 is more strongly adsorbed at the Pt_3 cluster than SOF_2 is, through chemisorption in both scenarios. This strong binding is reflected in a significant shift in sheet

conductance upon uptake of either analyte. Most importantly, the binding energies stay relatively low, suggesting that the sensor can be regenerated thermally, which is essential for practical cyclic operation. The HOMO/LUMO mapping supports these observations: When SOF_2 is adsorbed, the frontier orbitals shift towards the Pt_3 binding site, whereas SO_2F_2 adsorption leads to the entire LUMO moving onto the SO_2F_2 molecule, consistent with strong net electron transfer from the substrate to the adsorbate and a high degree of chemical interaction. This study has shown that Pt_3-$MoSe_2$ is a promising candidate for GIS partial discharge monitoring, and it broadly supports the principle of multi-atom noble metal cluster functionalization as an extension of the single-atom strategies explored for MoS_2 systems.

How Pt surface modification affects MoS_2 has been experimentally confirmed at the device level. Park et al. [38] first deposited two-dimensional MoS_2 films on Si wafers using metal-organic chemical vapor deposition, then used electron-beam evaporation with shadow masks to define interdigitated Au/Ti contacts; finally, the sensors were benchmarked against undecorated controls (Fig. 5). At 70 ppm H_2S, Pt nanoparticle decoration increased the sensitivity of the MoS_2 sensor by a factor of 4.25 relative to the undecorated sensor. It also lowered the limit of detection from 30 to 5 ppm at room temperature. The improvement comes from the Schottky barrier at the Pt/MoS_2 contact, which intensifies p-type gating and enhances sensitivity to electron-donating analytes. This experimentally supported mechanism demonstrates the applicability of Pt surface functionalization to sensing SF_6 decomposition gases. Taken together, Au- and Pt-functionalized systems enhance gas adsorption and charge transfer through noble-metal active sites, but they exhibit different target-gas preferences. Au-based systems have mainly been investigated for SO_2F_2 adsorption, whereas Pt-based systems cover SOF_2 and SO_2F_2 theoretically and have also been experimentally evaluated for H_2S sensing. Further work should optimize noble-metal loading and dispersion and evaluate selectivity, recovery, and long-term stability In an SF_6 background.

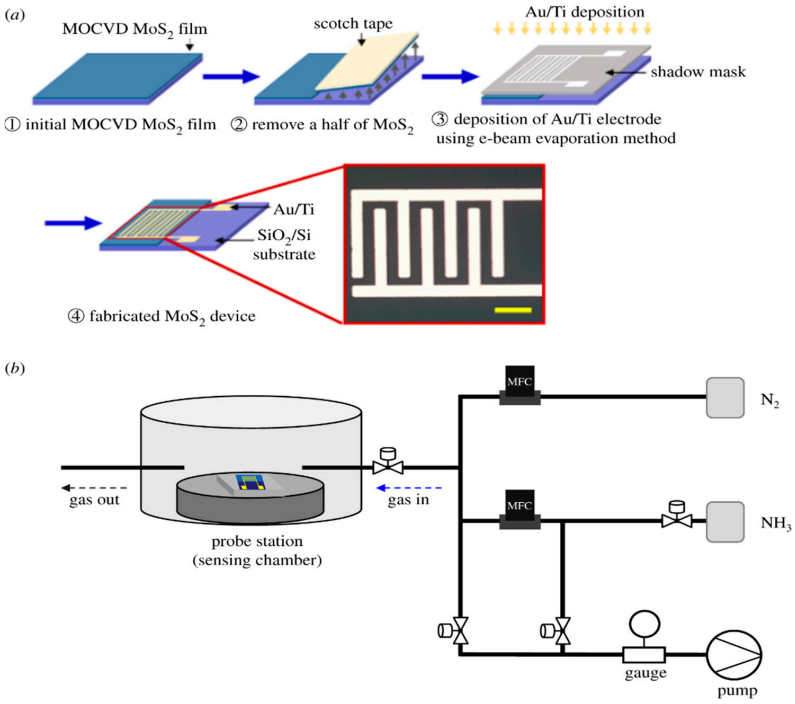

Figure 5: (**a**) Schematic illustration of the fabrication of MoS_2 gas sensor and an optical image of interdigitated electrode on the MoS_2. The scale bar is 50 μm. (**b**) Schematic illustration of the gas-sensing system. Reproduced from Ref. [38].

3.2.2 Non-Noble Metal Atom Modification

Despite the impressive sensing performance of MoS_2 decorated with Au, Pt, and Pd, large-scale production is a significant challenge due to the rarity and high cost of these metals. Growing interest in modifying surfaces with earth-abundant transition metals has fueled a rising number of strategies for using these metals and metal oxide nanoparticles as active modifiers. These methods have shown that they can match or even go beyond the performance levels of systems that have been modified with noble metals in key sensing metrics, while drastically reducing raw material costs [39,40].

Liu et al. [41] were among the first to investigate Ir-modified MoS_2 monolayers supported on surfaces to identify decomposition gases. Researchers utilized a 4×4 supercell of MoS_2 as their computational platform, generating three distinct coordination geometries around the Ir atoms. An examination of how the electrons are arranged in the system showed strong hybridization between the Ir 5p orbitals and the Mo 4d orbitals in energy levels from −7.0 to 2.0 eV. This hybridization significantly lowered the system's band gap from 2.088 eV to 0.398 eV, which substantially boosted its electrical conductivity. Regarding the energetics of gas binding, the adsorption energies at the Ir center for H_2S, SO_2, and SOF_2 were −2.323 eV, −1.757 eV, and −1.492 eV, respectively. All these values are well within the chemisorption regime, far surpassing the weak van der Waals binding seen on the unmodified surface. Among the three analytes, H_2S induces the largest charge transfer between the gas molecule and the Ir-modified MoS_2 substrate and exhibits the strongest adsorption. At a given temperature, the rate of thermal desorption is fastest for SOF_2 and slowest for H_2S (Fig. 6). All three target species are adsorbed, which significantly alters the surface work function, leading to a different transduction mechanism and a resistive channel.

Recent advances in atomic-scale modification for sensing SF_6 decomposition gases have focused mainly on surface anchoring. Su et al. [42] anchored W atoms on the MoS_2 basal plane and then evaluated adsorption of the four main fault gases on the resulting W–MoS_2 platform. The binding energies spanned a broad and well-defined range (−1.795 eV for H_2S and −2.481 to −4.874 eV for SO_2, SOF_2, and SO_2F_2). Mechanistically, the W-derived states hybridize with the MoS_2 conduction band, boosting the density of states around the Fermi level and thereby increasing the baseline conductivity. The partial density of states (PDOS) decomposition shows that SO_2F_2 binds nearly perfectly between the W d-states, while the interaction with H_2S is relatively weak due to the intrinsic strength of the W-S bond. Comparison of the two systems reveals complementary roles for the surface modifiers. Ir creates a highly active adsorption center, particularly for H_2S, while W broadens the adsorption range to include all four major SF_6 decomposition gases. Because both studies remain at the theoretical stage, the next step is to fabricate corresponding sensing devices and determine whether strong adsorption can be combined with acceptable recovery and repeatability.

3.3 Composite Structures

3.3.1 Metal Oxide Composite Structures

In the MoS_2/metal oxide composite architecture, the p-n or n-n heterojunction at the MoS_2/metal oxide (MOx) interface is the principal source of the improved sensing performance. Band-edge mismatch across the interface creates a space-charge region that alters the baseline resistance, free-carrier density, and activation barrier for gas-solid reactions. The result is a multiplicative amplification of sensitivity relative to either component alone. For detecting SF_6 faults, the two most critical diagnostic positions are occupied by H_2S and SO_2: H_2S reveals thermal fault conditions, while SO_2 is the primary indicator of partial discharge

activity. Achieving high sensitivity and high selectivity for both gases is therefore the central objective of research into metal oxide composite sensing materials based on MoS_2 [43,44].

The sulfur affinity of MoS_2 forms the foundation for H_2S detection, and when this is combined with other metal oxides to form heterojunctions, the transduction signal is boosted. Metal-oxide/MoS_2 heterojunctions enhance H_2S sensing through interfacial charge redistribution and an increased density of adsorption sites. Zhang et al. [45] reported room-temperature H_2S detection using CuO/MoS_2 nanocomposites prepared by hydrothermal synthesis and subsequently assembled into bilayer films via layer-by-layer (LbL) electrostatic self-assembly. The composite was confirmed by XRD, XPS, SEM, and TEM analyses. In a typical n-n architecture, Singh and Sharma [46] developed MoS_2/WO_3 nanocomposites (Fig. 7). The process was simplified to two steps. Lowering the operating temperature, the sensor was strongly biased toward hydrogen sulfide over ethanol at 320°C, while maintaining high repeatability and long-term stability.

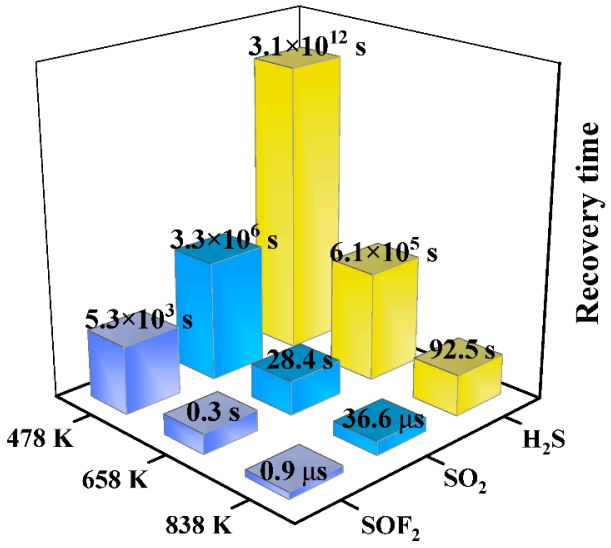

Figure 6: The predicted recovery time of various optimized systems. Reproduced from Ref. [41].

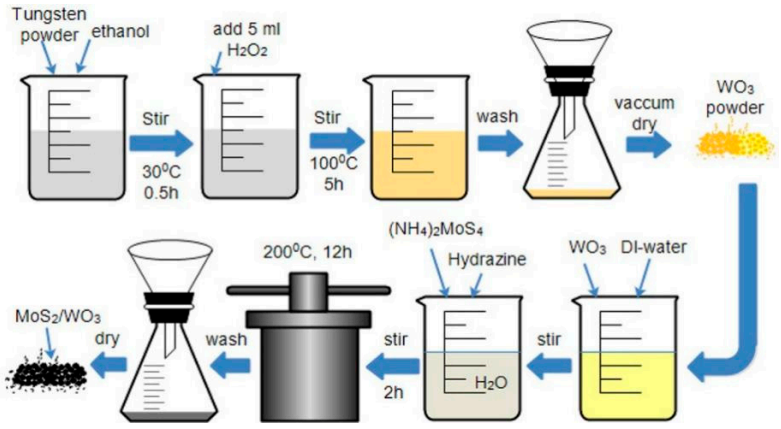

Figure 7: Schematic representation of two-step synthesis route for the MoS_2/WO_3 nanocomposite. Reproduced from Ref. [46].

Sadaf et al. [47] employed a p-n junction structure by integrating p-type NiO with MoS_2, creating a range of MoS_2-NiO nanocomposites. This was achieved through a straightforward hydrothermal method.

Among the compositions tested, the MNO-10 mixture showed the best response to H_2S. It attained a peak Rg/Ra ratio of 6.3 at 10 ppm, roughly triple the value of bare NiO, with a 2 ppm detection threshold, response and recovery times of 50 and 20 s, operational stability for 28 days, and reproducibility across six consecutive test cycles (Fig. 8a–d). The key mechanistic feature of MoS_2 here is that it simultaneously increases the active surface area, multiplies adsorption sites, and reinforces the p-n-junction depletion field, all alongside NiO. Sadaf et al. [48] then replaced NiO with spinel $ZnCo_2O_4$ as the p-type oxide partner. The resulting MZCO-6 sensor showed a Ra/Rg ratio of 6.6 at 10 ppm H_2S, approximately three times that of pristine $ZnCo_2O_4$. The MoS_2-NiO system was slower to respond compared to the composite based on $ZnCo_2O_4$.

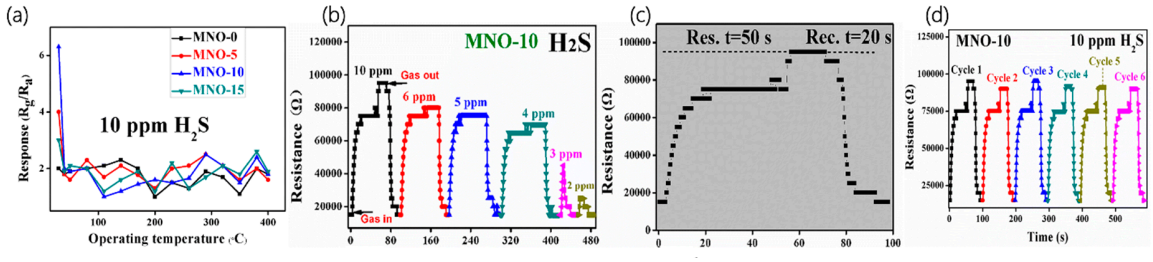

Figure 8: H_2S-sensing performance of MoS_2–NiO sensors: (**a**) responses of MNO-0, MNO-5, MNO-10, and MNO-15 toward 10 ppm H_2S at different operating temperatures; (**b**) dynamic resistance curves of MNO-10 toward 2–10 ppm H_2S at room temperature; (**c**) response and recovery behavior of MNO-10 toward 10 ppm H_2S at room temperature; and (**d**) six-cycle reproducibility of MNO-10 toward 10 ppm H_2S at room temperature. Panels (**a**–**d**) were adapted from Ref. [47].

In the MoS_2/ZnO heterojunction, the energy difference between the two n-type semiconductors causes electrons to move from MoS_2 to the lower energy ZnO conduction band, thereby creating a built-in electric field that simultaneously boosts SO_2 molecule chemisorption and speeds up carrier transport across the junction. Using a two-step protocol, Tang et al. first grew vertically aligned ZnO nanorod (NR) networks by hydrothermal treatment and subsequently combined the ZnO NRs with MoS_2 nanoflowers through physical mixing to fabricate the ZnO NR/MoS_2 NF heterojunction. In air, the resulting sensor exhibited response and recovery times of 52 and 5 s, respectively, toward 30 ppm SO_2 at 250°C. Under an SF_6 background, the corresponding values changed to 11 s and 7 s, respectively. Crucially, this study uncovered that in an SF_6 atmosphere, F_2^- species participate in the SO_2 sensing reaction, creating a transduction pathway absent in air. This mechanistic finding is relevant to the development of MoS_2-based sensors for realistic GIS monitoring [49].

First-principles simulations reveal that MoS_2/ZnO composites can detect both SO_2 and H_2S and that structural modification can improve analyte selectivity. The study of van der Waals heterojunctions using DFT [50] looked at how they adsorb toxic gases, especially SO_2 and hydrogen sulfide (H_2S). At the interface, adsorption of the two analytes changes from physisorption to chemisorption, with adsorption energies of −0.98 and −0.88 eV, respectively. Adding zinc oxide shifts the Fermi level and changes the electrostatic surface potential of MoS_2 by creating a band-like offset. In a similar vein, the presence of adsorption sites for both SO_2 and H_2S is what makes this response so strong and resistant. Building on that foundation, Gao et al. [51] first pioneered a deliberate defect engineering strategy. They constructed four structurally different functionalized heterojunctions: MoS_2/ZnO(VZn), MoS_2/ZnO(B), MoS_2/ZnO(N), and MoS_2/ZnO(Si). They systematically investigated gas adsorption on both sides of each heterojunction and also considered the simultaneous adsorption of multiple gas molecules to clarify the corresponding reaction pathways. Their calculations showed that MoS_2/ZnO(N) had the strongest affinity for H_2S, whereas MoS_2/ZnO(VZn)

exhibited the most distinctive adsorption response, highlighting the potential of defect engineering for multi-component SF_6 fault-gas discrimination. The reported metal-oxide composites follow two related but distinct development paths. CuO/MoS_2, NiO/MoS_2, and $MoS_2/ZnCo_2O_4$ mainly enhance H_2S sensing through interfacial charge redistribution, while ZnO/MoS_2 extends this approach to SO_2 detection and demonstrates the potential of defect regulation for improving selectivity. Direct comparison among these materials remains difficult because their operating temperatures and response definitions differ. Therefore, unified testing standards are needed.

3.3.2 Carbon-Based Composite Structures

The physics of how MoS_2/carbon composites are made sensitive differs markedly from that of metal oxide systems. Instead of relying on built-in space-charge fields, the signal is amplified through van der Waals interlayer coupling between MoS_2 and graphene or reduced graphene oxide (rGO), which enables swift electron transfer across the heterojunction. The exposed terminations of the edges and sulfur vacancy sites of MoS_2 offer high-energy binding sites for incoming gas molecules. The sp^2-hybridized π-electron network of graphene or rGO functions as a low-resistance conduction highway, rapidly transporting the charge perturbation induced by the adsorption to external measurement contacts. Hydrogen sulfide is the main analyte targeted in experimental studies on this class of composites [52].

Liu et al. [53] developed an rGO–PDDA–MoS_2 sensing chip by assembling 2D MoS_2 with graphene oxide (GO) using PDDA, drop casting the composite onto interdigitated electrodes, and subsequently reducing GO *in situ* with hydrazine vapor. PDDA intercalation and MoS_2 stacking increased the GO interlayer spacing from 0.77 to 1.44 nm, improving gas accessibility and helping prevent rGO restacking after reduction. At room temperature, the sensor showed good selectivity and stability toward H_2S, with a calculated detection limit of 3 ppb. Hingangavkar et al. [54] explored an alternative pairing in which graphene oxide (GO) played the role of carbon scaffold, instead of its reduced form. The composites were fabricated using a clean hydrothermal method and then characterized by XRD, Raman spectroscopy, XPS, field-emission scanning electron microscopy (FESEM), and impedance spectroscopy. They reported that the resulting sensor reliably detected H_2S at 28°C and exhibited high stability and cycle-to-cycle reproducibility. Unlike rGO, GO retains a dense population of oxygen-bearing functional groups that provide additional anchoring sites for H_2S, strengthening the room-temperature response. Jin et al. [55] adopted a different approach, pairing MoS_2 with pristine graphene (G) exfoliated by low-cost mechanical cleavage. They then performed parallel DFT calculations to compare H_2S adsorption on MoS_2 heterojunctions with that on bare MoS_2 monolayers. The heterojunction setup gave off a markedly stronger H_2S binding, which can be attributed to interfacial charge coupling that boosts chemisorption at the active sites, resulting in a sensitive room-temperature H_2S response. The use of mechanical exfoliation also makes the process compatible with standard semiconductor microfabrication workflows, which is beneficial for scalable device production.

As for MoS_2/CNT composites, Jha et al. [56] showed that sub-ppm SO_2 could be detected at room temperature by using carboxyl-functionalized MWCNTs as a conducting scaffold for MoS_2 nanosheet assembly. Acid treatment introduced carboxyl (–COOH) groups onto the MWCNTs; the functionalized MWCNTs were then combined with MoS_2 to form composite sensing films, which were characterized by TEM, XRD, and XPS. This enhancement works in three steps: sulfur vacancies and exposed edge sites on MoS_2 act as preferential sites for attaching SO_2 molecules; the abundant –COOH groups on the walls of MWNT provide additional Lewis acid-base binding sites; and a one-dimensional MWNT scaffold creates a percolating low-resistance pathway. The device registered SO_2 response values ranging from 0.22 to 1.81% across a concentration range of 0.5–3 ppm, operating stably at a bias voltage of just 100 mV. This stands

among the earliest reported experimental validations of ppb-class room-temperature SO_2 detection in a MoS_2/CNT platform (Fig. 9). Zhang et al. [57] proposed V-functionalized graphene/MoS_2 heterojunctions (GMV) and used DFT to benchmark their adsorption of the four principal SF6 decomposition gases against that of pristine graphene/MoS2 (GM). Whereas GM binds the target molecules only through weak van der Waals forces with negligible charge transfer, GMV strengthens the adsorption of H_2S, SO_2, and SOF_2 through the active V center. SO_2 showed the most negative binding energy (−0.388 eV) and the shortest adsorption distance; at room temperature and a modulation frequency of 1 × 106 Hz, its predicted desorption time was 2.43 s, indicating potential sensor regenerability. The key implication of this work is that V functionalization elevates the graphene/MoS_2 platform from a passive physisorption medium to a chemically active sensor capable of covering all four main SF_6 decomposition gases.

In summary, experimental investigations of MoS_2/carbon composite systems for SF_6 decomposition gas sensing have concentrated on room-temperature ultrasensitive H_2S detection, with rGO-PDDA-MoS_2 and MoS_2-GO platforms driving the H_2S detection threshold into the sub-ppb range; on the computational side, V-atom functionalization of graphene/MoS_2 heterojunctions has extended theoretical coverage to all four principal SF_6 decomposition gases. Relative to metal-oxide composite systems, however, MoS_2/carbon-based composites for SF_6 decomposition gas sensing remains at an early stage of development, indicating substantial room for further exploration.

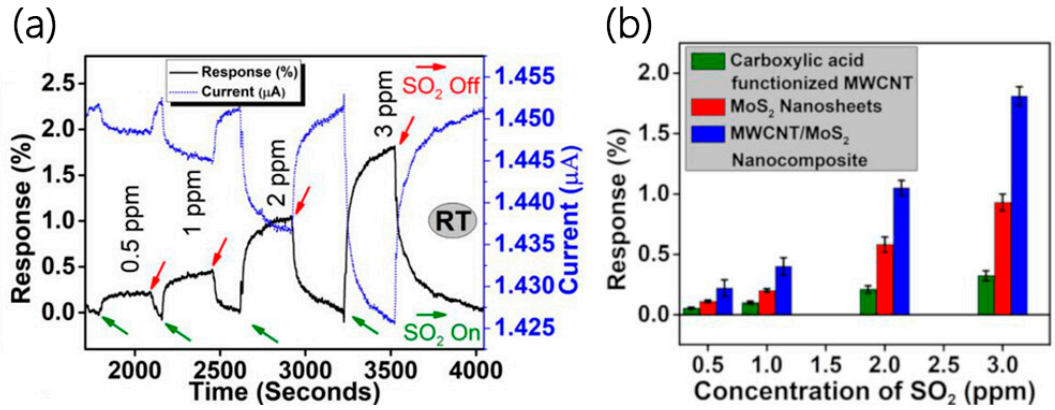

Figure 9: (**a**) Dynamic response of the device to 0.5–3 ppm SO_2 at room temperature; (**b**) Comparison of MoS_2, Carboxylic acid-functionalized MWCNT, and nanocomposite based SO_2 gas sensor. Adapted from Ref. [56].

3.3.3 Multi-Component Composite Structures

The metal oxide/MoS_2 and carbon/MoS_2 systems covered in Sections 3.3.1 and 3.3.2 are both binary heterojunction architectures. A single junction interface, however, provides only one degree of freedom for simultaneously tuning sensitivity, selectivity, and transient response kinetics, which motivates the development of multi-component composite strategies that introduce two or more heterogeneous interfaces into a single sensing material. Progress in multi-component MoS_2-based systems has been reported for both H_2S and SO_2.

To detect H_2S, Wu et al. [58] built a ternary MoS_2 octahedra/ZnO-Zn_2SnO_4 nanoparticle system through hydrothermal synthesis, yielding three compositions with 0, 5, and 10 wt.% MoS_2 loading (labeled MS-ZNO-0, MS-ZNO-5, and MS-ZNO-10). At approximately 30°C, the 5 wt% MoS_2 composite exhibited a response ratio of approximately 4 at 2 ppm H_2S. The quantification threshold was 0.05 ppm (Ra/Rg = 1.8). The mixture was stable over a period of 35 days and showed good reproducibility across five consecutive cycles (Fig. 10a,b). The performance increase can be attributed to three cooperative contributions: the large surface area of

the octahedral MoS_2 morphology, the formation of n-n heterojunctions at the MoS_2/ZnO-Zn_2SnO_4 contact planes, and an increased population of surface oxygen species (Fig. 10c). A composition-dependent optimum was identified, with MS-ZNO-5 showing superior performance to MS-ZNO-10, highlighting that excessive MoS_2 passivates the active sites of ZnO-Zn_2SnO_4, which is a key design principle for multi-component systems.

For SO_2 detection, a Pt–TiO_2/MoS_2 ternary nanocomposite was fabricated by layer-by-layer electrostatic assembly to provide multiple signal-enhancement mechanisms. Device testing showed that the sensor exhibited a relatively high response to SO_2, good selectivity over the other tested gases, and good stability. Parallel DFT calculations further backed up the superior affinity for SO_2. In this system, TiO_2 forms a wide-bandgap oxide scaffold that is decorated with a dense array of surface hydroxyl groups, which promote initial SO_2 physisorption. Pt nanoparticles then act as catalytic activation nodes, lowering the activation barrier for SO_2 chemisorption at the TiO_2/MoS_2 interface. This study offers a representative example of how the combination of experimental device fabrication and DFT mechanistic validation can be integrated for MoS_2-based multifunctional SO_2 sensors. In short, the multi-component composite architecture uses two or more heterojunction interfaces within a single MoS_2 system to perform both H_2S and SO_2 detection. Compared to binary systems, it offers more design freedom for performance optimization. The biggest obstacle ahead is to achieve precise control over both the composition and the interface of the components, so they work together synergistically rather than in competition [59].

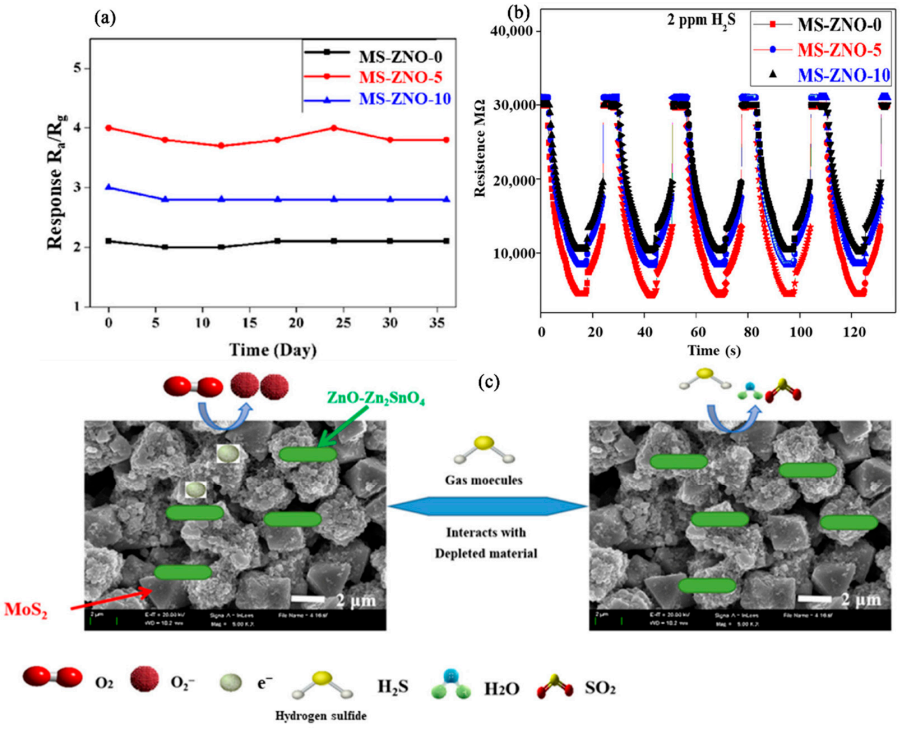

Figure 10: (**a**) The stability graph; (**b**) Reproducibility graphs of MS-ZNO-0, MS-ZNO-5 and MS-ZNO-10; (**c**) Diagram of gas sensing mechanism. Adapted from Ref. [58].

4 Applications of MoS_2-Based Materials in SF6 Decomposition Gas Detection

The degradation of insulation in GIS equipment leads to the fragmentation of SF_6, releasing four key fault marker gases: H_2S, SO_2, SOF_2, and SO_2F_2. In the last few years, MoS_2-based sensing materials have

made significant progress in device development for all four targets, moving steadily from first-principles predictions to fabricated and experimentally verified sensor prototypes with genuine engineering potential for GIS health monitoring. Table 1 shows the key performance metrics and detection limits across the main material systems discussed.

Recent advances in detection limits have been driven by developments in p-n junctions. Sensors based on In_2O_3@MoS_2 exhibit a detection limit of 3 ppb and function fully after 50 bending cycles [60]. In 2026, Verma et al. [34] reported that a 5 at% Pd-doped MoS_2 thin-film sensor synthesized via APCVD achieved an H_2S limit of detection of 0.3 ppb. MoS_2–NiO and MoS_2/ZnO–Zn_2SnO_4 sensors have also achieved ppm- or sub-ppm-level H_2S detection under ambient or near-ambient conditions.

For SO_2 sensing, Tang et al. [49] subjected ZnO NR/MoS_2 NF heterojunction devices to rigorous testing under both laboratory air and genuine SF_6 background conditions. The sensor showed response and recovery times of 11 and 7 s, respectively, when exposed to 30 ppm SO_2 in an SF_6 background. First-principles calculations also showed that the interface between ZnO and MoS_2 adsorbs SO_2 more strongly than either material alone. According to the authors, this study provided the first experimental validation of a MoS_2-based SO_2 sensor in an SF_6 background. In this regard, Gond et al. [61] utilized magnetron sputtering to deposit Fe_2O_3/MoS_2 composite films, achieving detection across a wide range of concentrations, from 0.1–100 ppm, with a detection limit of 22.8 ppb. Compared with H_2S and SO_2, experimental validation of MoS_2-based sensors for SOF_2 and SO_2F_2 remains limited. DFT calculations showed that Pt_2–MoS_2 exhibited particularly strong adsorption toward two SOF_2 molecules, with a calculated adsorption energy of −2.65 eV. The associated conductivity response was inferred from changes in the density of states and HOMO–LUMO gap [36]. DFT calculations further showed that W-modified MoS_2 exhibited adsorption energies of −3.478 and −4.874 eV for SOF_2 and SO_2F_2, respectively, with the adsorption-strength order SO_2F_2 > SOF_2 > SO_2 > H_2S. This represents the most complete theoretical coverage of MoS_2-based SF_6 decomposition gas sensing to date.

Overall, these materials have progressed toward practical detection of SF_6 decomposition gases, although most remain at the laboratory stage. The sensors for H_2S and SO_2 have already reached ppb-level sensitivity, but the SO_2 platform has only been verified under simulated SF_6 conditions. A key technical challenge is the simultaneous differentiation of multiple analytes. Because several characteristic gases may be released concurrently during GIS faults, combining multichannel MoS_2 sensors with data-fusion and machine-learning algorithms could enable their simultaneous identification and quantification in online GIS monitoring systems.

Table 1: Summary of MoS_2-based sensor research: techniques and detection limits.

Sensing Material	Target Gas	Adsorption Energy (eV)	LOD	Ref.
Pristine MoS_2	SO_2, SOF_2	−0.33 to −0.21	—	[19]
Si-MoS_2	H_2S, SOF_2	—	—	[23]
P-MoS_2	H_2S	—	—	[24]
B@MoS_2	H_2S, SO_2, SOF_2, SO_2F_2	−1.66 to −0.49	—	[19]
C/N-MoS_2	H_2S, SO_2, SOF_2, SO_2F_2	—	—	[19]
O/Se/Te-MoS_2	H_2S, SO_2, SOF_2, SO_2F_2	—	—	[19]
Ga-MoS_2	SO_2, SO_2F_2	—	—	[25]
Ni-MoS_2	H_2S, SO_2	H_2S: −1.319; SO_2: −1.382	—	[28]
Pd-MoS_2 (theoretical)	SOF_2, SO_2F_2	—	—	[29]
Co-MoS_2	SOF_2, SO_2F_2	—	—	[30]
Pt-MoS_2 (doped)	SO_2, SOF_2	—	—	[31]
Au-MoS_2 (doped)	SO_2, SOF_2, SO_2F_2	—	—	[31]

Table 1: *Cont.*

Sensing Material	Target Gas	Adsorption Energy (eV)	LOD	Ref.
Sc-MoS_2	H_2S, SO_2, SOF_2, SO_2F_2	—	—	[32]
Pd-MoS_2 (exp., APCVD)	H_2S	—	0.3 ppb	[34]
Au-MoS_2 (modified)	SO_2F_2	—	—	[35]
Pt-MoS_2 (modified)	SOF_2, SO_2F_2	—	—	[36]
Pt_2-MoS_2	SOF_2, SO_2F_2	—	—	[36]
Pt_3-$MoSe_2$	SOF_2, SO_2F_2	—	—	[37]
Pt NPs/MoS_2	H_2S	—	5 ppm	[38]
Ir-MoS_2	H_2S, SO_2, SOF_2	H_2S: −2.323; SO_2: −1.757; SOF_2: −1.492	—	[41]
W-MoS_2	H_2S, SO_2, SOF_2, SO_2F_2	H_2S: −1.795; SO_2: −2.481; SOF_2: −3.478; SO_2F_2: −4.874	—	[42]
CuO/MoS_2	H_2S	—	—	[45]
MoS_2/WO_3	H_2S	—	—	[46]
MoS_2-NiO (MNO-10)	H_2S	—	2 ppm	[47]
MoS_2-$ZnCo_2O_4$ (MZCO-6)	H_2S	—	—	[48]
ZnO NR/MoS_2 NF	SO_2	SO_2: −0.98	—	[49]
MoS_2/ZnO heterojunction	SO_2, H_2S	SO_2: −0.98; H_2S: −0.88	—	[50]
MoS_2/ZnO(N)	H_2S	—	—	[51]
MoS_2/ZnO(VZn) (defect eng.)	SO_2	—	—	[51]
In_2O_3@MoS_2	H_2S	—	3 ppb	[60]
Fe_2O_3/MoS_2	SO_2	—	22.8 ppb	[61]
rGO-PDDA-MoS_2	H_2S	—	3 ppb	[53]
MoS_2-GO	H_2S	—	—	[54]
Graphene/MoS_2 (G/MoS_2)	H_2S	—	—	[55]
MWCNT/MoS_2	SO_2	—	—	[56]
V-doped Graphene/MoS_2 (GMV)	H_2S, SO_2, SOF_2, SO_2F_2	SO_2: −0.388	—	[57]
MoS_2/ZnO-Zn_2SnO_4 (MS-ZNO-5)	H_2S	—	0.05 ppm	[58]
Pt-TiO_2/MoS_2	SO_2	—	—	[59]

Table 1 focuses on MoS_2-based sensing of the four conventional SF_6 decomposition gases, whereas recent studies have also considered condition monitoring in reduced-SF_6 and SF_6-free insulating media. Das et al. validated ultrasonic density monitoring in both pure SF_6 and an 80% N_2/20% SF_6 mixture, reporting a linear response and a worst-case response time of 80 s under tests up to 50 kV AC and 70 kV DC [62]. Although this mixture reduces the SF_6 inventory, it still contains SF_6, and its streamer behavior remains dependent on electric-field non-uniformity [63]. For the fluoronitrile alternative, a 20% C_3F_7CN/80% CO_2 mixture, where C_3F_7CN is another notation for C_4F_7N, passed dielectric type tests in a full-scale 420/550 kV GIL/GIB demonstrator [64]. However, its impulse breakdown voltage was lower than that of SF_6 under weakly non-uniform fields, and protrusion tests showed a shorter time-to-breakdown for identical defects [65,66]. Its diagnostic gas profile is also different: long-path FTIR detected C_3F_6, CO, and COF_2 after overheating, while an SnO_2/rGO–SnO_2/Co_3O_4 sensor array provided complementary detection of CO and C_4F_7N. Therefore, the H_2S, SO_2, SOF_2, and SO_2F_2 calibration models summarized in Table 1 cannot be directly transferred to C_4F_7N/CO_2-insulated equipment. Pd-modified MoS_2 and Cu_3-modified MoS_2 have been proposed by DFT for C_4F_7N leakage and C_2N_2 detection, respectively, but experimental validation under practical mixed-gas conditions remains necessary [67,68].

In addition to changes in the insulating-gas medium, practical GIS condition assessment also requires monitoring of moisture and gas leakage. Excessive moisture in GIS vessels may promote condensation, corrosion, and reactions between H_2O and discharge-generated low-fluorine species, thereby affecting

both insulation reliability and the composition and concentration ratios of characteristic gases used for fault diagnosis. SF_6 leakage reduces gas density and pressure and may consequently impair the dielectric and arc-quenching performance of the equipment. In addition, variations in moisture, pressure, and background-gas composition can influence sensor response and concentration calibration, reducing the accuracy of SF_6 decomposition-gas analysis if these factors are not properly compensated. Moisture and leakage measurements therefore provide essential complementary information for interpreting MoS_2 sensor signals. Recent ppm-scale moisture-sensing technologies are compared in Table 2, and their integration with decomposition-gas and gas-density monitoring can support more reliable GIS condition assessment, condition-based maintenance, and substation automation.

Table 2: Comparison of complementary moisture and SF_6 leakage/state-monitoring technologies for GIS.

Sensor	Measured Quantity	Moisture Range (ppmv)	Ref.
Porous Al_2O_3/FTO sensor	Capacitive sensing	246–725	[69]
DFB-laser QEPAS sensor	Photoacoustic spectroscopy	1400–23,700	[70]
Multilayer GO-coated TFBG sensor	Optical-fiber sensing	13–1081	[71]
UHF–MEMS composite sensor	Integrated gas-state sensing	0–1000	[72]

5 Conclusions and Perspectives

This review organizes the current research landscape of MoS_2-based composite materials for SF_6 decomposition gas detection. It covers three structural modification strategies: lattice-level doping, surface-species functionalization, and heterojunction composite construction. It also assesses the suitability of these approaches for detecting the four main GIS fault-indicator gases: H_2S, SO_2, SOF_2, and SO_2F_2. For lattice doping, both non-metallic and metallic substituents consistently shift the adsorption of SF_6 byproducts from the physisorptive to the chemosorptive territory. Different types of doping have unique analyte coverage profiles and selectivity fingerprints, which can be leveraged in complementary ways. To functionalize the surface, noble metal anchoring relies on strong d-orbital hybridization to enhance chemisorption, while transition metal surface modification can expand the four-gas coverage and enable thermally reversible desorption. For composite architectures, the ZnO nanorod/MoS_2 nanoflower (ZnO NR/MoS_2 NF) heterojunction exhibited measurable responses to SO_2 concentrations down to 500 ppb in both air and an SF_6 background at 250°C. At room temperature, the reported H_2S detection limits of the MoS_2–NiO and MoS_2–$ZnCo_2O_4$ sensors were 2 ppm and 0.5 ppm, respectively. At the device level, the lowest detected limits for MoS_2-based sensors are now as low as 0.3 ppb for H_2S and 22.8 ppb for SO_2, which already meet the threshold requirements for warning about pre-fault GIS insulation.

Despite the progress made, several critical hurdles must be cleared before MoS_2-based sensing platforms can be deployed reliably in GIS field applications. The following priority areas deserve focused attention:

(1) Research on SOF_2 and SO_2F_2 is primarily conducted at the level of first principles. The key challenge here is transforming these computational results into fabricated sensor devices and then thoroughly verifying their performance.

(2) Because multiple characteristic decomposition gases may coexist under realistic GIS fault conditions, multichannel MoS_2 sensor arrays integrated with machine-learning pattern-recognition algorithms are needed for concurrent analyte identification and quantification.

(3) The majority of the reported sensing experiments used clean synthetic air as the carrier gas. The effect of compounding environmental factors, such as SF_6 background atmosphere, humidity, and

high-voltage electric field, on sensor stability and selectivity is still poorly understood and deserves systematic investigation.

(4) Sensors used in embedded GIS systems have to be drastically reduced in size and power consumption. Bridging the gap between laboratory prototypes and ruggedized, field-ready instruments is a crucial engineering step.

With continued progress in materials synthesis and processing, advances in multi-component cooperative sensing architectures, and the growing convergence of this platform with artificial intelligence and data analytics, MoS_2-based sensing is well-positioned to move from lab demonstrations to real-time, multi-parameter online monitoring of GIS insulation degradation, ultimately building a more robust technological foundation for safe power grid operation.

Acknowledgement: Not applicable.

Funding Statement: This work was supported by the Science and Technology Project of the Yunnan Provincial Department of Science and Technology (Grant No. 202305AF150123).

Author Contributions: Huo Ye—Conceptualization, data curation, investigation, writing, original draft; Jiantong Li—Data curation, investigation, writing, review & editing; Lingna Xu—Writing, review & editing, supervision. All authors reviewed and approved the final version of the manuscript.

Availability of Data and Materials: No new datasets were generated in this study. All information supporting the findings of this review is available in the published literature cited in the article.

Ethics Approval: Not applicable.

Conflicts of Interest: The authors declare no conflicts of interest.

References

1. Toigo C, Vu-Cong T, Jacquier F, Girodet A. Partial discharge behavior of protrusion on high voltage conductor in GIS/GIL under high voltage direct current: Comparison of SF_6 and SF_6 alternative gases. IEEE Trans Dielectr Electr Insul. 2020;27(1):140–7. [CrossRef].
2. Zhuang Y, Hu X, Tang B, Wang S, Cui A, Hou K, et al. Effects of SF_6 decomposition components and concentrations on the discharge faults and insulation defects in GIS equipment. Sci Rep. 2020;10(1):15039. [CrossRef].
3. Tang J, Liu F, Zhang X, Meng Q, Zhou J. Partial discharge recognition through an analysis of SF_6 decomposition products part 1: Decomposition characteristics of SF_6 under four different partial discharges. IEEE Trans Dielectr Electr Insul. 2012;19(1):29–36. [CrossRef].
4. Mahdi AS, Abdul-Malek Z, Arshad RN. SF_6 decomposed component analysis for partial discharge diagnosis in GIS: A review. IEEE Access. 2022;10:27270–88. [CrossRef].
5. Yang L, Wang S, Chen C, Zhang Q, Sultana R, Han Y. Monitoring and leak diagnostics of sulfur hexafluoride and decomposition gases from power equipment for the reliability and safety of power grid operation. Appl Sci. 2024;14(9):3844. [CrossRef].
6. Purnomoadi AP, Mor AR, Smit JJ. Spacer flashover in Gas Insulated Switchgear (GIS) with humid SF_6 under different electrical stresses. Int J Electr Power Energy Syst. 2020;116:105559. [CrossRef].
7. Dong M, Zhang C, Ren M, Albarracín R, Ye R. Electrochemical and infrared absorption spectroscopy detection of SF_6 decomposition products. Sensors. 2017;17(11):2627. [CrossRef].
8. Fan X, Li L, Zhou Y, Tang N, Zou Z, Li X, et al. Online detection technology for SF_6 decomposition products in electrical equipment: A review. IET Sci Meas Tech. 2018;12(6):707–11. [CrossRef].
9. Burman D, Raha H, Manna B, Pramanik P, Guha PK. Substitutional doping of MoS_2 for superior gas-sensing applications: A proof of concept. ACS Sens. 2021;6(9):3398–408. [CrossRef].

10. Liu H, Zhang S, Cheng Q, Wang L, Wang S. A mini review on the recent progress of MoS_2-based gas sensors. Catal Lett. 2024;154(4):1375–84. [CrossRef].
11. Kumar S, Mirzaei A, Kumar A, Hoon Lee M, Ghahremani Z, Kim TU, et al. Nanoparticles anchored strategy to develop 2D MoS_2 and $MoSe_2$ based room temperature chemiresistive gas sensors. Coord Chem Rev. 2024;503:215657. [CrossRef].
12. Liu CH, Palanisamy S, Chen SM, Wu PS, Yao L, Lou BS. Mechanism of formation of SF_6 decomposition gas products and its identification by GC-MS and electrochemical methods: A mini review. Int J Electrochem Sci. 2015;10(5):4223–31. [CrossRef].
13. Qian G, Peng Q, Wang H, Wang S, Dai W. Morphological characteristics of molybdenum disulfide and current application on detecting SF_6 decomposing products. Front Mater. 2020;7:580245. [CrossRef].
14. Zeng F, Li H, Cheng H, Tang J, Liu Y. SF_6 decomposition and insulation condition monitoring of GIE: A review. High Volt. 2021;6(6):955–66. [CrossRef].
15. Khan Q, Refaat SS, Abu-Rub H, Toliyat HA. Partial discharge detection and diagnosis in gas insulated switchgear: State of the art. IEEE Electr Insul Mag. 2019;35(4):16–33. [CrossRef].
16. Dai D, Wang X, Zhao Y, Zhang Y, Zhang J. GIS insulation fault diagnosis based on detection of SF_6 decomposition products. In: Proceedings of the 2017 9th International Conference on Measuring Technology and Mechatronics Automation (ICMTMA); 2018 Jan 14–15; Changsha, China. p. 60–7. [CrossRef].
17. Zeng F, Tang J, Fan Q, Pan J, Zhang X, Yao Q, et al. Decomposition characteristics of SF_6 under thermal fault for temperatures below 400°C. IEEE Trans Dielectr Electr Insul. 2014;21(3):995–1004. [CrossRef].
18. Zhong L, Ji S, Wang F, Sun Q, Chen S, Liu J, et al. Theoretical study of the chemical decomposition mechanism and model of Sulfur hexafluorid (SF_6) under corona discharge. J Fluor Chem. 2019;220:61–8. [CrossRef].
19. Tursun M, Liu Y, Yumaier A. Boosting the adsorption and sensing performance of MoS_2 for SF_6 decomposition gases by non-metal atom doping: A DFT study. RSC Adv. 2026;16(4):3021–33. [CrossRef].
20. Zhao S, Xue J, Kang W. Gas adsorption on MoS_2 monolayer from first-principles calculations. Chem Phys Lett. 2014;595–596:35–42. [CrossRef].
21. Maksymiuk J, Wrona IA, Szczesniak R, Durajski AP. Tunable optical and electronic properties of monolayer MoS_2 via substitutional doping. Surf Sci. 2025;761:122788. [CrossRef].
22. Suh J, Tan TL, Zhao W, Park J, Lin DY, Park TE, et al. Reconfiguring crystal and electronic structures of MoS_2 by substitutional doping. Nat Commun. 2018;9(1):199. [CrossRef].
23. Gui Y, Liu D, Li X, Tang C, Zhou Q. DFT-based study on H_2S and SOF_2 adsorption on Si-MoS_2 monolayer. Results Phys. 2019;13:102225. [CrossRef].
24. Szary MJ. MoS_2 doping for enhanced H_2S detection. Appl Surf Sci. 2021;547:149026. [CrossRef].
25. Hou W, Mi H, Peng R, Peng S, Zeng W, Zhou Q. First-principle insight into Ga-doped MoS_2 for sensing SO_2, SOF_2 and SO_2F_2. Nanomaterials. 2021;11(2):314. [CrossRef].
26. Gao J, Zhang Y, Li X, Shi G, Zhang Y. Quantitative detection of multicomponent SF_6 decomposition products based on Fourier transform infrared spectroscopy combined with CARS-ELM algorithm. IEEE Trans Instrum Meas. 2022;71:2514708. [CrossRef].
27. Zhang X, Yan J, Zhang Y, Cheng L, Bian C, Chen X. Infrared spectrum analysis and quantitative detection of SF_6 characteristic decomposition components SO_2F_2 and SOF_2. IEEE Trans Dielectr Electr Insul. 2022;29(4):1316–23. [CrossRef].
28. Wei H, Gui Y, Kang J, Wang W, Tang C. A DFT study on the adsorption of H_2S and SO_2 on Ni doped MoS_2 monolayer. Nanomaterials. 2018;8(9):646. [CrossRef].
29. Li T, Gui Y, Zhao W, Tang C, Dong X. Palladium modified MoS_2 monolayer for adsorption and scavenging of SF_6 decomposition products: A DFT study. Phys E Low Dimens Syst Nanostruct. 2020;123:114178. [CrossRef].
30. Gui Y, Wang Y, Duan S, Tang C, Zhou Q, Xu L, et al. *Ab initio* study of SOF_2 and SO_2F_2 adsorption on co-MoS_2. ACS Omega. 2019;4(2):2517–22. [CrossRef].
31. Chen D, Zhang X, Tang J, Cui H, Li Y. Noble metal (Pt or Au)-doped monolayer MoS_2 as a promising adsorbent and gas-sensing material to SO_2, SOF_2 and SO_2F_2: A DFT study. Appl Phys A. 2018;124(2):194. [CrossRef].
32. Li B, Zhou Q, Peng R, Liao Y, Zeng W. Adsorption of SF_6 decomposition gases (H_2S, SO_2, SOF_2 and SO_2F_2) on Sc-doped MoS_2 surface: A DFT study. Appl Surf Sci. 2021;549:149271. [CrossRef].

33. Zhang D, Wu J, Li P, Cao Y. Room-temperature SO_2 gas-sensing properties based on a metal-doped MoS_2 nanoflower: An experimental and density functional theory investigation. J Mater Chem A. 2017;5(39):20666–77. [CrossRef].
34. Verma VK, Patel C, Mukherjee S, Bhowmick S, Upadhyay SN, Kumar V, et al. Ultrasensitive and selective room temperature H_2S detection using Pd-doped MoS_2 synthesized via APCVD. Sens Actuators B Chem. 2026;447:138812. [CrossRef].
35. Gui Y, Chen W, Lu Y, Tang C, Xu L. Au catalyst-modified MoS_2 monolayer as a highly effective adsorbent for SO_2F_2 gas: A DFT study. ACS Omega. 2019;4(7):12204–11. [CrossRef].
36. Gui Y, Shi J, Yang P, Li T, Tang C, Xu L. Platinum modified MoS_2 monolayer for adsorption and gas sensing of SF_6 decomposition products: A DFT study. High Volt. 2020;5(4):454–62. [CrossRef].
37. Qian H, Deng J, Xie Z, Pan Z, Zhang J, Zhou H. Adsorption and gas sensing properties of the Pt_3-$MoSe_2$ monolayer to SOF_2 and SO_2F_2. ACS Omega. 2020;5(13):7722–8. [CrossRef].
38. Park J, Mun J, Shin JS, Kang SW. Highly sensitive two-dimensional MoS_2 gas sensor decorated with Pt nanoparticles. R Soc Open Sci. 2018;5(12):181462. [CrossRef].
39. Zhu LY, Ou LX, Mao LW, Wu XY, Liu YP, Lu HL. Advances in noble metal-decorated metal oxide nanomaterials for chemiresistive gas sensors: Overview. Nanomicro Lett. 2023;15(1):89. [CrossRef].
40. Gao DH, Yu QC, Kebeded MA, Zhuang YY, Huang S, Jiao MZ, et al. Advances in modification of metal and noble metal nanomaterials for metal oxide gas sensors: A review. Rare Met. 2025;44(3):1443–96. [CrossRef].
41. Liu H, Wang F, Hu K, Li T, Yan Y, Li J. The adsorption and sensing performances of Ir-modified MoS_2 monolayer toward SF_6 decomposition products: A DFT study. Nanomaterials. 2021;11(1):100. [CrossRef].
42. Su C, Gui Y, Li J, Tao J, Zhang J, Zhang Q. Selective sensing of SF_6 decomposition products on W-modified MoS_2: A first-principles study for electrical fault diagnosis. Colloids Surf A Physicochem Eng Asp. 2026;741:140276. [CrossRef].
43. Meng FJ, Xin RF, Li SX. Metal oxide heterostructures for improving gas sensing properties: A review. Materials. 2023;16(1):263. [CrossRef].
44. Goel N, Kunal K, Kushwaha A, Kumar M. Metal oxide semiconductors for gas sensing. Eng Rep. 2023;5(6):e12604. [CrossRef].
45. Zhang D, Wu J, Cao Y. Ultrasensitive H_2S gas detection at room temperature based on copper oxide/molybdenum disulfide nanocomposite with synergistic effect. Sens Actuators B Chem. 2019;287:346–55. [CrossRef].
46. Singh S, Sharma S. Temperature-based selective detection of hydrogen sulfide and ethanol with MoS_2/WO_3 composite. ACS Omega. 2022;7(7):6075–85. [CrossRef].
47. Sadaf S, Zhang H, Akhtar A. MoS_2-NiO nanocomposite for H_2S sensing at room temperature. RSC Adv. 2023;13(41):28564–75. [CrossRef].
48. Sadaf S, Zhang H, Chen D, Akhtar A. Highly sensitive room temperature H_2S gas sensor based on the nanocomposite of MoS_2–$ZnCo_2O_4$. ACS Omega. 2023;8(49):47023–33. [CrossRef].
49. Tang M, Zhang D, Sun Y, Wang Z, Xi G, Chen Q, et al. Chemiresistive detection of SO_2 in SF_6 decomposition products based on ZnO nanorod/MoS_2 nanoflower heterojunctions: Experimental and first-principles investigations. Sens Actuators B Chem. 2024;403:135170. [CrossRef].
50. Gao J, Gao K, Miao L, Ding J, Chen H, Fu H, et al. First principle investigation on gas sensing properties of MoS_2/ZnO heterojunction. Microchem J. 2024;206:111414. [CrossRef].
51. Gao K, Ding J, Gao J, Fan J, Chen H. Highly selective adsorption of MoS_2/ZnO heterojunctions for SO_2 and H_2S gas molecules: A DFT study. Mater Today Commun. 2025;42:111266. [CrossRef].
52. Cho B, Yoon J, Lim SK, Kim AR, Kim DH, Park SG, et al. Chemical sensing of 2D graphene/MoS_2 heterostructure device. ACS Appl Mater Interfaces. 2015;7(30):16775–80. [CrossRef].
53. Liu X, He Z, Xu S, Wu J, Wu J. Assembly of 2D-MoS_2 with graphene layer for highly sensitive and selective gas detection at room temperature. Sens Actuators B Chem. 2022;367:132185. [CrossRef].
54. Hingangavkar GM, Kadam SA, Ma YR, Bandgar SS, Mulik RN, Patil VB. MoS_2-GO hybrid sensor: A discerning approach for detecting harmful H_2S gas at room temperature. Chem Eng J. 2023;472:144789. [CrossRef].
55. Jin Y, Yu Z, Li P, Manoharan M, Zhuang X. Room-temperature H_2S gas sensor based on graphene/MoS_2 heterojunction: Experimental and theoretical insights. J Mater Sci. 2026;61(10):6814–27. [CrossRef].

56. Jha RK, Nanda A, Bhat N. Sub-ppm sulfur dioxide detection using MoS_2 modified multi-wall carbon nanotubes at room temperature. Nano Sel. 2022;3(1):98–107. [CrossRef].
57. Zhang A, Chang X, Liu T, An J, Liu X, Cui Y, et al. A DFT investigation of SF_6 decomposition products' adsorption on V-doped graphene/MoS_2 heterostructures. Chemistry. 2026;8(4):50. [CrossRef].
58. Wu D, Akhtar A. Ppb-level hydrogen sulfide gas sensor based on the nanocomposite of MoS_2 octahedron/ZnO-Zn_2SnO_4 nanoparticles. Molecules. 2023;28(7):3230. [CrossRef].
59. Zhang D, Pang M, Wu J, Cao Y. Experimental and density functional theory investigation of Pt-loaded titanium dioxide/molybdenum disulfide nanohybrid for SO_2 gas sensing. New J Chem. 2019;43(12):4900–7. [CrossRef].
60. Huo Y, Qiu L, Wang T, Yu H, Yang W, Dong X, et al. P-N Heterojunction formation: Metal Sulfide@Metal Oxide Chemiresistor for ppb H_2S Detection from Exhaled Breath and Food Spoilage at Flexible Room Temperature. ACS Sens. 2024;9(6):3433–43. [CrossRef].
61. Gond R, Barala S, Shukla P, Bassi G, Kumar S, Kumar M, et al. Fe_2O_3-functionalized MoS_2 nanostructure sensor for high-sensitivity and low-level SO $_2$ detection. ACS Sens. 2025;10(5):3412–22. [CrossRef].
62. Das SD, Kumar S, Biswal GR, Islam T. Condition monitoring of sulfur hexafluoride gas-insulated switchgear vessel using smart ultrasonic sensor. IEEE Trans Instrum Meas. 2026;75:9701608. [CrossRef].
63. Sun Y, Li Z, Liu J, Gao H, Zhang L, Wang S, et al. Effects of electric field nonuniformity on DC positive streamer discharge of SF_6/N_2 mixed gas. IEEE Trans Dielectr Electr Insul. 2024;31(4):2019–28. [CrossRef].
64. Loizou L, Chen L, Liu Q, Cotton I, Waldron M, Owens JG. Technical viability of retro-filling C_3F_7CN/CO_2 gas mixtures in SF_6-designed gas insulated lines and busbars at transmission voltages. IEEE Trans Power Deliv. 2020;35(5):2394–402. [CrossRef].
65. Ranjan P, Oancea M, Han Q, Bahdad FO, Onoufriou C, Seltzer-Grant M, et al. Partial discharge monitoring of C3F7CN/CO_2 mixture retrofilled in gas insulated busbar. IEEE Trans Power Deliv. 2024;39(6):3212–22. [CrossRef].
66. Loizou L, Chen L, Liu Q, Waldron M. Lightning impulse breakdown characteristics of SF_6 and 20% C_3F_7CN/80% CO_2 mixture under weakly non-uniform electric fields. IEEE Trans Dielectr Electr Insul. 2020;27(3):848–56. [CrossRef].
67. Yan Y, Luo Y, Li Y, Zhang Y, Wu P, Tang J, et al. Transition metal (Au, Ag, Pt, Pd, Ni) doped MoS_2 as gas sensing materials for C_4F_7N leakage detection: A comparative study. Surf Interfaces. 2024;44:103625. [CrossRef].
68. Li C, Chen P, Yu Y, Li C. Cu_γ (γ = 1–3)-modified MoS_2 monolayer as a gas sensor for detecting C_4F_7N and its decomposition components. Nanomaterials. 2022;12(16):2829. [CrossRef].
69. Zargar ZH, Akram KJ, Biswal GR, Islam T. A linear capacitive sensor for ppm moisture measurement in SF_6 gas-insulated switchgear. IEEE Trans Instrum Meas. 2021;70:1–8. [CrossRef].
70. Yin X, Dong L, Wu H, Gao M, Zhang L, Zhang X, et al. Compact QEPAS humidity sensor in SF_6 buffer gas for high-voltage gas power systems. Photoacoustics. 2022;25:100319. [CrossRef].
71. Wang Y, Ma G, Gao X, Ji J, Xu B, Du H, et al. Enhanced detection of SF_6 gas moisture concentration in gas-insulated switchgear utilizing tilted fiber Bragg grating coated with multilayer graphene oxide films. IEEE Trans Instrum Meas. 2024;73:1–9. [CrossRef].
72. Chen H, Wang H, Zhang Z, Guo R, Han X, Zhang X, et al. A novel composite sensor for UHF partial discharge and gas state measurement in GIS. IEEE Trans Instrum Meas. 2024;73:1501410. [CrossRef].